Atmos. Meas. Tech., 9, 6025–6034, 2016
www.atmos-meas-tech.net/9/6025/2016/
doi:10.5194/amt-9-6025-2016
© Author(s) 2016. CC Attribution 3.0 License.

Atmospheric Measurement Techniques Open Access EGU

The AOTF-based NO_2 camera

Emmanuel Dekemper, Jurgen Vanhamel, Bert Van Opstal, and Didier Fussen

Royal Belgian Institute for Space Aeronomy (BIRA-IASB), Avenue Circulaire 3, 1180 Brussels, Belgium

Correspondence to: Emmanuel Dekemper (emmanuel.dekemper@aeronomie.be)

Received: 15 July 2016 – Published in Atmos. Meas. Tech. Discuss.: 15 August 2016
Revised: 22 November 2016 – Accepted: 24 November 2016 – Published: 15 December 2016

Abstract. The abundance of NO_2 in the boundary layer relates to air quality and pollution source monitoring. Observing the spatiotemporal distribution of NO_2 above well-delimited (flue gas stacks, volcanoes, ships) or more extended sources (cities) allows for applications such as monitoring emission fluxes or studying the plume dynamic chemistry and its transport. So far, most attempts to map the NO_2 field from the ground have been made with visible-light scanning grating spectrometers. Benefiting from a high retrieval accuracy, they only achieve a relatively low spatiotemporal resolution that hampers the detection of dynamic features.

We present a new type of passive remote sensing instrument aiming at the measurement of the 2-D distributions of NO_2 slant column densities (SCDs) with a high spatiotemporal resolution. The measurement principle has strong similarities with the popular filter-based SO_2 camera as it relies on spectral images taken at wavelengths where the molecule absorption cross section is different. Contrary to the SO_2 camera, the spectral selection is performed by an acousto-optical tunable filter (AOTF) capable of resolving the target molecule's spectral features.

The NO_2 camera capabilities are demonstrated by imaging the NO_2 abundance in the plume of a coal-fired power plant. During this experiment, the 2-D distribution of the NO_2 SCD was retrieved with a temporal resolution of 3 min and a spatial sampling of 50 cm (over a $250 \times 250\,m^2$ area). The detection limit was close to 5×10^{16} molecules cm^{-2}, with a maximum detected SCD of 4×10^{17} molecules cm^{-2}. Illustrating the added value of the NO_2 camera measurements, the data reveal the dynamics of the NO to NO_2 conversion in the early plume with an unprecedent resolution: from its release in the air, and for 100 m upwards, the observed NO_2 plume concentration increased at a rate of 0.75–1.25 g s^{-1}. In joint campaigns with SO_2 cameras, the NO_2 camera could also help in removing the bias introduced by the NO_2 interference with the SO_2 spectrum.

1 Introduction

Nitrogen oxides ($NO_x = NO + NO_2$) play a key role in the air quality of the boundary layer. While NO is produced in combustion processes (transport, thermal power plants, etc.), NO_2 mainly appears through the reaction of NO with O_3 or HO_2. Eventually, the photolysis of NO_2 releases an oxygen atom and a NO molecule. To a good approximation, the balance of NO and NO_2 is kept constant through this cycle of photo-chemical reactions, which substantiates the widespread use of the NO_x family concept (Seinfeld and Pandis, 2006). Considering the relative ease of measuring NO_2 with visible-light spectroscopy, NO_x budgets are often inferred based on NO_2 measurements and the photochemical equilibrium assumption.

The most common NO_2 remote sensing techniques rely on the differential optical absorption spectroscopy (DOAS), which is based on the fitting of radiance spectra with the effective absorption cross section of interfering species (e.g., Platt, 1994). If equipped with a 2-D sensor array, these instruments disperse the light spectrum along one dimension and record its spatial variation along the other. Building a complete hyperspectral image requires an incremental depointing of the instantaneous field of view (FOV) or a translation of the whole instrument. Typical examples of both applications can be found in Heue et al. (2008) or Lohberger et al. (2004). While the DOAS technique is well validated in terms of accuracy and sensitivity, the need for scanning the scene hampers the detection of dynamic processes. As the scene is sampled slice by slice, the final image does not show a great temporal consistency: different rows (or columns, depending

on the scanning direction) are temporally disconnected from each other. The time gap can reach several minutes between both edges of the scene.

There are situations where high spatiotemporal resolution is needed. In volcanology, for instance, the so-called SO_2 cameras are now increasingly complementing the measurements performed with classical dispersive techniques like grating spectrometers (Mori and Burton, 2006; Bluth et al., 2007). Their concept is based on taking spectral images of the plume through two interference filters. One filter selects a narrow band of the incident spectrum around 310 nm, where SO_2 is still strongly absorbing, while the other one captures the light around 330 nm, where almost no more absorption takes place. The main advantages are a typical temporal resolution of 1 Hz, the capability to capture dynamic features such as puffs in the plume and the possibility to determine the plume speed from the sequence of images. The disadvantages are the interference by the plume aerosols caused by the coarse spectral resolution and the need for regular recalibration with reference cells filled with SO_2 to account for changes of illumination conditions (Kern et al., 2010). More recent concepts now use the combined information of a spectrometer with the camera spectral images (Lübcke et al., 2013), which yields a greater measurement accuracy.

We present a new instrument, a spectral imager dedicated to measuring the 2-D NO_2 field above finite sources like thermal power plants, industrial complexes, cities, volcanoes, etc. The measurement principle is close to the SO_2 camera: snapshots at two wavelengths emphasize the presence of NO_2 by taking advantage of absolute differences in the molecule absorption cross section. Contrary to the SO_2 cameras which use interference filters, the new instrument relies on an acousto-optical tunable filter (AOTF) to provide the spectral information. The AOTF can offer sufficient spectral resolution to resolve the structures of the NO_2 spectrum. The ability to discriminate between weak and strong absorption within a few nanometers virtually cuts out any sensitivity to aerosol scattering and changes of solar angles. Potential applications include urban and industrial pollution monitoring, emission fluxes estimation, satellite-product validation and volcanic plume chemistry.

2 Instrument concept

The AOTF-based NO_2 camera springs from the ALTIUS instrument (atmospheric limb tracker for the investigation of the upcoming stratosphere; Fussen et al., 2016). ALTIUS is a space mission project aimed at the retrieval of atmospheric species concentration profiles with a global geographical coverage and a high vertical resolution. Its primary scientific objective is to measure ozone, but NO_2, aerosols, H_2O, CH_4, polar stratospheric and noctilucent clouds, and other minor species will be measured as well. Measurements will be performed in two different geometries: limb scattering and occultations (Sun, Moon, stars, planets). To address the problem of tangent height registration of previous limb scatter instruments, a spectral imager concept based on a tunable filter has been selected. During the feasibility study, a prototype of the visible (VIS) channel (440–800 nm) was built from commercially available parts. The detailed description of this prototype is given in Dekemper et al. (2012). We will only point out the key features of the concept.

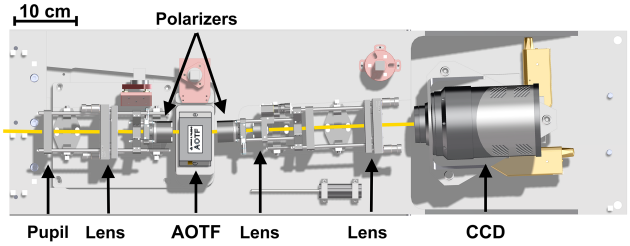

Figure 1. Optical layout of the NO_2 camera seen from top. Light propagates from left to right through a pupil and a lens doublet, a polarizer selecting vertically polarized light, the AOTF, a second cross-oriented polarizer, two lens doublets and the detector.

The instrument images a 6° square FOV onto a Princeton Instrument Pixis 512B peltier-cooled CCD detector (512 × 512 pixels). The optical layout (Fig. 1) is linear with an intermediate focal plane located close to the AOTF. To preserve the spectral homogeneity across the image, the design is made telecentric by placing an iris at the object focal point of the first lens. This ensures an identical propagation angle of all light rays through the AOTF.

The most important part of this NO_2 camera concept is the AOTF (Chang, 1974). AOTFs have been used in many areas requiring spectral images (agriculture, food industry, fluorescence spectroscopy, etc.) but received little attention from the atmospheric remote sensing community. The working principle is based on the interaction of light and sound in a birefringent crystal (see Fig. 2). By the momentum matching of the optical and acoustic waves, a narrow portion of the light spectrum is diffracted into a slightly different direction (a few degrees). If the incident radiation is linearly polarized, the diffracted beam will leave the crystal with the orthogonal polarization. The spatial and polarimetric dissociations can be combined to achieve very efficient extinction of the unwanted spectrum.

The wave vector's matching condition (Fig. 2) creates a monotonic relationship between the light wavelength and the sound frequency. The acoustic wave is launched into the crystal by a piezoelectric transducer bonded to one of its facets. Hence, selecting a particular wavelength λ simply requires us to drive the transducer to the matching frequency $F(\lambda)$. The AOTF spectral transmission function (STF) closely follows a sinc^2 shape. The amplitude of the STF, which determines the filter diffraction efficiency (DE), is controlled by the acoustic power $P_a(\lambda)$, which also exhibits

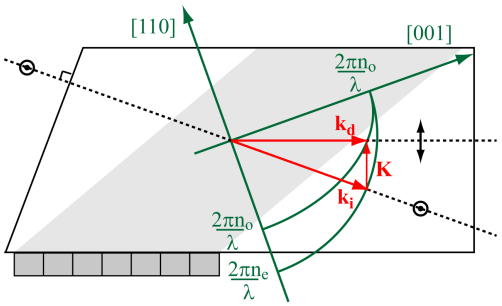

Figure 2. Schematics of the acousto-optic interaction in an AOTF (top view). The gray area depicts the acoustic field created by the piezoelectric transducer bonded to a lateral face of the TeO_2 crystal. The momentum phase matching of the incident ($\boldsymbol{k}_i$) and diffracted ($\boldsymbol{k}_d$) photons with the acoustic wave ($\boldsymbol{K}$) is represented in the $[\bar{1}10]$ crystallographic frame. The phase matching takes advantage of the medium birefringence: incident and diffracted light beams have orthogonal polarizations and different propagation directions, which facilitates their selection.

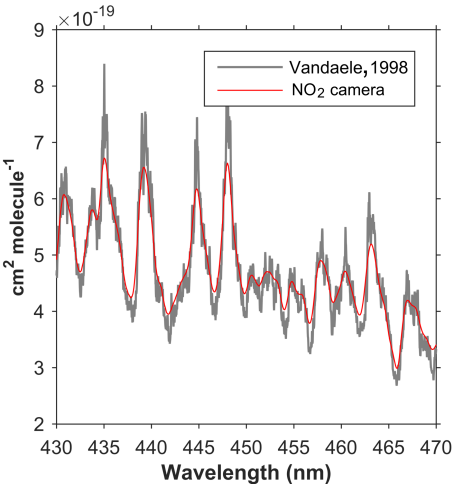

Figure 3. NO_2 absorption cross section measured with a Fourier transform spectrometer (gray line; Vandaele et al., 1998) and with this NO_2 camera in the laboratory (red line). At 450 nm, the spectral resolution of both datasets are 0.04 and 0.6 nm respectively.

a smooth wavelength dependence. The transducer length defines the length of the acousto-optic interaction, which directly affects the AOTF bandwidth: a short transducer will induce a larger passband and vice versa.

The parameters of an AOTF are defined by the crystal elastic and optical properties and by the propagation directions of light and sound in the frame of the crystal axes (Voloshinov et al., 2007). The AOTF we used was manufactured out of a TeO_2 crystal by the company Gooch & Housego (UK). It offers an aperture of $10 \times 10\,mm^2$ and a tuning range covering the visible spectrum. Laboratory characterization revealed a transparency better than 90 % and a DE better than 95 %. In the relevant spectral range for NO_2 measurements, i.e., around 450 nm, the STF showed a bandwidth of 0.6 nm. Typical driving frequencies were around 130 MHz, and less than 100 mW of acoustic power was needed in any circumstances. The theoretical number of resolvable spots at 450 nm is about 350 in the plane of acousto-optic interaction (horizon) and 700 in the vertical direction.

3 Measurement principle

There are strong similarities between the measurement principles of a filter-based SO_2 camera and an AOTF-based NO_2 camera: the FOV needs to be pointed towards the target region (e.g., a plume) while making sure that the background can still be seen in some areas of the image. Two spectral images of the scene are taken: one at a wavelength λ_s where there is strong absorption by the target species and another at a wavelength λ_w where there is weak absorption. In each image, the signal $S_{ij}(\lambda)$ (in e^-) recorded by pixel ij looking at the plume will be normalized by the background signal $S_0(\lambda)$ in order to quantify the extinction that took place during the crossing of the plume. The optical thickness τ_{ij} associated with the slant column density (SCD) of the target species observed in the FOV of pixel ij follows from the comparison of the normalized signals recorded at the two wavelengths.

The major difference comes from the capability of the AOTF-based NO_2 camera to resolve the fine structures of the absorption cross section σ_{NO_2} (Fig. 3). This allows choosing λ_s and λ_w very close to each other (a few nm), minimizing the interference by broadband absorbing and scattering species like aerosols.

3.1 Mathematical model

As AOTFs do not treat different polarizations identically, an AOTF-based NO_2 camera exhibits a strong polarization sensitivity. The polarization state of a stream of light is described by the Stokes vector $\boldsymbol{s} = (I, Q, U, V)^T$, where $I = I^h + I^v$ and $Q = I^h - I^v$, with I^h and I^v being the light intensity along the horizontal and vertical axes of a scene frame. U and V also refer to the orientation of the polarization ellipse but they will not be discussed further because they do not participate if the AOTF and its surrounding polarizers are well aligned.

When light passes through a polarizing part, its Stokes vector can be changed. A polarizing element is therefore represented by a 4×4 transfer matrix: the Mueller matrix $\mathbf{M}$. A chain of optical elements is represented by the product of their Mueller matrices. In our design, the light passes first through a vertical linear polarizer, then the AOTF, and finally a horizontal linear polarizer. The Stokes vector representing the light leaving the second polarizer is therefore given by $\boldsymbol{s}' = \mathbf{M}_{Ph} \cdot \mathbf{M}_{AOTF} \cdot \mathbf{M}_{Pv} \cdot \boldsymbol{s}$. The Mueller matrices of the ele-

ments are as follows:

$$\mathbf{M}_{\mathrm{AOTF}} = \frac{A}{2}\begin{pmatrix} 1 & -1 & 0 & 0 \\ 1 & -1 & 0 & 0 \\ 0 & 0 & 0 & 0 \\ 0 & 0 & 0 & 0 \end{pmatrix}, \tag{1}$$

$$\mathbf{M}_{\mathrm{Pv}} = \frac{1}{2}\begin{pmatrix} \eta_{\mathrm{e}}^2+\eta_{\mathrm{t}}^2 & \eta_{\mathrm{e}}^2-\eta_{\mathrm{t}}^2 & 0 & 0 \\ \eta_{\mathrm{e}}^2-\eta_{\mathrm{t}}^2 & \eta_{\mathrm{e}}^2+\eta_{\mathrm{t}}^2 & 0 & 0 \\ 0 & 0 & 2\eta_{\mathrm{e}}\eta_{\mathrm{t}} & 0 \\ 0 & 0 & 0 & 2\eta_{\mathrm{e}}\eta_{\mathrm{t}} \end{pmatrix}, \tag{2}$$

$$\mathbf{M}_{\mathrm{Ph}} = \frac{1}{2}\begin{pmatrix} \eta_{\mathrm{t}}^2+\eta_{\mathrm{e}}^2 & \eta_{\mathrm{t}}^2-\eta_{\mathrm{e}}^2 & 0 & 0 \\ \eta_{\mathrm{t}}^2-\eta_{\mathrm{e}}^2 & \eta_{\mathrm{t}}^2+\eta_{\mathrm{e}}^2 & 0 & 0 \\ 0 & 0 & 2\eta_{\mathrm{e}}\eta_{\mathrm{t}} & 0 \\ 0 & 0 & 0 & 2\eta_{\mathrm{e}}\eta_{\mathrm{t}} \end{pmatrix}, \tag{3}$$

where A is the amplitude of the AOTF STF (i.e., its DE, $0 \leq A \leq 1$), η_{t}^2 is the attenuation of the light intensity along the polarizer transmission axis, and η_{e}^2 is the attenuation along the extinction axis. Assuming that all three elements have their transmission and extinction axes well aligned, the total Mueller matrix of the camera is simply $\mathbf{M} = \eta_{\mathrm{t}}^4 \cdot \mathbf{M}_{\mathrm{AOTF}}$. As the detector only measures the total light intensity, the first element of the Stokes vector is the only meaningful quantity: $s'(1) = A \cdot \eta_{\mathrm{t}}^4 \cdot (I - Q)/2 = A \cdot \eta_{\mathrm{t}}^4 \cdot I^{\mathrm{v}}$. Hence, in the present configuration, the NO_2 camera is only sensitive to vertically polarized component of the light.

We now have a description of the light intensity which will be measured by the detector, but we still have to account for the transmittance of the lenses (T) and the quantum efficiency (QE) of the detector. These terms exhibit a smooth wavelength dependence. For the AOTF STF, one can use $\mathcal{F}(\lambda;\lambda_c) = A(\lambda_c) \cdot G(\lambda - \lambda_c)$, where G is essentially a sinc^2 function. Moreover, some parameters are susceptible to vary across the FOV, yielding a pixel-to-pixel variation. This is particularly true when image planes are located close to optical surfaces (mainly the AOTF and the detector). Finally, the electronic current (in $\mathrm{e}^-\ \mathrm{s}^{-1}$) found in pixel ij when the AOTF is tuned to λ_c is given by

$$\begin{aligned} C_{ij}(\lambda_c) &= \int A_{ij}(\lambda_c) \cdot \eta_{\mathrm{t}}^4(\lambda) \cdot I_{ij}^{\mathrm{v}}(\lambda) \cdot G(\lambda - \lambda_c) \\ &\quad \cdot T(\lambda) \cdot \mathrm{QE}_{ij}(\lambda)\,\mathrm{d}\lambda, \\ &\simeq A_{ij}(\lambda_c) \cdot \eta_{\mathrm{t}}^4(\lambda_c) \cdot T(\lambda_c) \cdot \mathrm{QE}_{ij}(\lambda_c) \\ &\quad \int I_{ij}^{\mathrm{v}}(\lambda) \cdot G(\lambda - \lambda_c)\,\mathrm{d}\lambda, \\ &= r_{ij}(\lambda_c) \int I_{ij}^{\mathrm{v}}(\lambda) \cdot G(\lambda - \lambda_c)\,\mathrm{d}\lambda. \end{aligned} \tag{4}$$

The decision to leave the smoothly varying parameters out of the integral is supported by the narrow passband of the AOTF (0.6 nm). Their product forms the instrument response at pixel ij and wavelength λ_c: $r_{ij}(\lambda_c)$. The remaining integral is simply the convolution of the vertically polarized incident light intensity with the AOTF STF.

Suppose now that pixel ij is looking through an optically thin plume. NO_2 and other species will absorb or scatter photons and decrease the background light intensity I_0^{v} according to the Beer–Lambert law of extinction:

$$I_{ij}^{\mathrm{v}}(\lambda) = I_0^{\mathrm{v}}(\lambda) \cdot \exp\left(-\tau_{\mathrm{NO_2}\,ij}(\lambda) - \tau_{*\,ij}(\lambda)\right), \tag{5}$$

where $\tau_{\mathrm{NO_2}\,ij}$ denotes the plume optical thickness caused by absorption by NO_2 along the light path ending on pixel ij, and $\tau_{*\,ij}$ is the effective optical thickness of all other chemical species and particles. Over the passband of the AOTF, one can consider $\tau_*(\lambda)$ as a constant value $\tau_*(\lambda_c)$ and replace $\tau_{\mathrm{NO_2}}(\lambda)$ by its weighted average:

$$\overline{\tau}_{\mathrm{NO_2}}(\lambda_c) = \frac{\int \tau_{\mathrm{NO_2}}(\lambda) \cdot G(\lambda - \lambda_c)\mathrm{d}\lambda}{\int G(\lambda - \lambda_c)\mathrm{d}\lambda}. \tag{6}$$

As the optical thickness is defined by the product of the trace gas SCD k with its absorption cross section σ, it is clear that $\overline{\tau}_{\mathrm{NO_2}}(\lambda_c) = k_{\mathrm{NO_2}} . \overline{\sigma}_{\mathrm{NO_2}}(\lambda_c)$. Under these assumptions, one can insert Eq. (5) into Eq. (4) and write for the pixel photoelectric current:

$$\begin{aligned} C_{ij}(\lambda_c) =& r_{ij}(\lambda_c) \cdot \exp\left(-\overline{\tau}_{\mathrm{NO_2}\,ij}(\lambda_c) - \tau_{*\,ij}(\lambda_c)\right) \\ &\cdot \int I_0^{\mathrm{v}}(\lambda) \cdot G(\lambda - \lambda_c)\,\mathrm{d}\lambda. \end{aligned} \tag{7}$$

In the meantime, other pixels have been looking at the unattenuated background intensity I_0. Suppose that one of them is pixel mn. According to Eq. (4), we have

$$C_{\mathrm{mn}}(\lambda_c) = r_{\mathrm{mn}}(\lambda_c) \cdot \int I_0^{\mathrm{v}}(\lambda) \cdot G(\lambda - \lambda_c)\,\mathrm{d}\lambda. \tag{8}$$

Averaging all these background-looking pixels yields the reference current associated with the background intensity:

$$C_0(\lambda_c) = r(\lambda_c) \cdot \int I_0^{\mathrm{v}}(\lambda) \cdot G(\lambda - \lambda_c)\,\mathrm{d}\lambda, \tag{9}$$

with r representing the average instrument response. Dividing C_{ij} by C_0 yields the transmittance of the plume alone:

$$T_{ij}(\lambda_c) = \frac{\frac{C_{ij}(\lambda_c)}{r_{ij}(\lambda_c)}}{\frac{C_0(\lambda_c)}{r(\lambda_c)}} = \exp\left(-\overline{\tau}_{\mathrm{NO_2}\,ij}(\lambda_c) - \tau_{*\,ij}(\lambda_c)\right). \tag{10}$$

If the spectral interval between λ_{w} and λ_{s} is small enough that the approximation $\tau_*(\lambda_{\mathrm{w}}) = \tau_*(\lambda_{\mathrm{s}})$ holds, then the ratio of the transmittances $T(\lambda_{\mathrm{w}})/T(\lambda_{\mathrm{s}})$ is a quantity which only depends on the NO_2 content of the plume. Introducing the relative instrument response at pixel ij, $\rho_{ij}(\lambda) = r_{ij}(\lambda)/r(\lambda)$, we find

$$\begin{aligned} \frac{T_{ij}(\lambda_{\mathrm{w}})}{T_{ij}(\lambda_{\mathrm{s}})} &= \frac{\frac{C_{ij}(\lambda_{\mathrm{w}})}{C_0(\lambda_{\mathrm{w}})\rho_{ij}(\lambda_{\mathrm{w}})}}{\frac{C_{ij}(\lambda_{\mathrm{s}})}{C_0(\lambda_{\mathrm{s}})\rho_{ij}(\lambda_{\mathrm{s}})}} \\ &= \exp\left(\overline{\tau}_{\mathrm{NO_2}\,ij}(\lambda_{\mathrm{s}}) - \overline{\tau}_{\mathrm{NO_2}\,ij}(\lambda_{\mathrm{w}})\right). \end{aligned} \tag{11}$$

Finally, the NO_2 SCD subtended by the area of the plume observed by pixel ij follows by taking the logarithm of the

ratio of transmittances:

$$k_{\mathrm{NO_2}\,ij} = \frac{1}{\overline{\sigma}_{\mathrm{NO_2}}(\lambda_\mathrm{s}) - \overline{\sigma}_{\mathrm{NO_2}}(\lambda_\mathrm{w})} \cdot \ln\left(\frac{T_{ij}(\lambda_\mathrm{w})}{T_{ij}(\lambda_\mathrm{s})}\right). \quad (12)$$

Clearly, the best sensitivity is reached by maximizing the differential optical thickness when selecting λ_w and λ_s.

3.2 Ancillary data

Equations (11) and (12) show that the NO_2 SCD can be obtained from a combination of measurements (the detector signal), cross-section data and the knowledge of the instrument response. In the results presented below, the cross section is taken from Vandaele et al. (1998). For the ρ_{ij} coefficients, an ad hoc method was set up to build a synthetic flat field. Taking advantage of a cloudy weather (100 % cloudiness), long-exposure frames (10 s) were captured at the required wavelengths looking at zenith. The mean image obtained from tens of such frames constitutes the instrument response to a synthetic, radiometrically flat scene. This allows us to remove wavelength-dependent nonuniformities which can be relatively pronounced in, e.g., the AOTF.

Determining the photoelectric current strictly proportional to the signal (i.e., C_{ij} and C_0) implies that voltage offset, dark current and stray light have been subtracted from the raw data. In this respect, AOTFs offer a unique feature: one can turn them off. This is simply done by bringing the acoustic wave amplitude to 0. An image acquired in these conditions contains anything but the real signal (i.e., dark current, offset, stray light). Using D_{ij} and D_{ij}^{off} to represent the raw signal of pixel ij (in digital numbers, DN) when the AOTF is turned on or off respectively, the photo-electric signal is given by

$$S_{ij} = \frac{D_{ij} - D_{ij}^{\mathrm{off}}}{\gamma}, \quad (13)$$

where γ is the sensor gain (in DN/e$^-$). The only precaution is to take these dark images regularly because the stray light is a function of the general illumination conditions (e.g., solar angles) and it will vary with local time.

3.3 Data averaging and multiple image doublets

It is often necessary to repeat the measurements in order to average out transient features and increase the signal-to-noise ratio. Assuming that only the plume optical transmission varies, we can write a time-dependent version of Eq. (7):

$$C_{ij}(\lambda_c, t) = r_{ij}(\lambda_c) \cdot \exp\left(-\overline{\tau}_{\mathrm{NO_2}\,ij}(\lambda_c, t) - \tau_{*\,ij}(\lambda_c, t)\right) \cdot \int I_0^\mathrm{v}(\lambda) \cdot G(\lambda - \lambda_c)\,\mathrm{d}\lambda. \quad (14)$$

The time-averaged optical thickness $\tau(\lambda, \bar{t})$ can be obtained from the geometric mean of the consecutive images:

$$\begin{aligned}
&\sqrt[N]{\prod_{k=1}^{N} C_{ij}(\lambda_c, t_k)} \\
&= r_{ij}(\lambda_c) \cdot \exp\left(-\frac{1}{N}\sum_{k=1}^{N} \overline{\tau}_{\mathrm{NO_2}\,ij}(\lambda_c, t_k) + \tau_{*\,ij}(\lambda_c, t_k)\right) \\
&\quad \cdot \int I_0^\mathrm{v}(\lambda) \cdot G(\lambda - \lambda_c)\,\mathrm{d}\lambda. \\
&= r_{ij}(\lambda_c).\exp\left(-\overline{\tau}_{\mathrm{NO_2}\,ij}(\lambda_c, \bar{t}) - \tau_{*\,ij}(\lambda_c, \bar{t})\right) \\
&\quad \cdot \int I_0^\mathrm{v}(\lambda).G(\lambda - \lambda_c)\,\mathrm{d}\lambda. \quad (15)
\end{aligned}$$

Another means of increasing the reliability of the measurements is to use different doublets, i.e., pairs of λ_w and λ_s. If the transmittance is known for several doublets, their product strengthens the NO_2 SCD retrieval by providing information from multiple spectral regions. If $\Delta\sigma_{\mathrm{NO_2}} = \overline{\sigma}_{\mathrm{NO_2}}(\lambda_\mathrm{s}) - \overline{\sigma}_{\mathrm{NO_2}}(\lambda_\mathrm{w})$, then for two doublets we have for the SCD

$$k_{\mathrm{NO_2}\,ij} = \frac{1}{\Delta\sigma_{\mathrm{NO_2}}^{(1)} + \Delta\sigma_{\mathrm{NO_2}}^{(2)}} \cdot \ln\left(\frac{T_{ij}(\lambda_{\mathrm{w}1}) \cdot T_{ij}(\lambda_{\mathrm{w}2})}{T_{ij}(\lambda_{\mathrm{s}1}) \cdot T_{ij}(\lambda_{\mathrm{s}2})}\right). \quad (16)$$

This approach can potentially attenuate a bias in one of the measurements.

3.4 Error budget and instrument sensitivity

One can work out Eq. (12) with the classical first-order Taylor expansion approximation to determine the uncertainty on the NO_2 SCD. This approach will require estimates of the uncertainty on the photon counts C_{ij}, on the background signal C_0, on the relative instrument response ρ_{ij} and on the cross-section data $\sigma_{\mathrm{NO_2}}$. These estimates are not always easily obtained, and we briefly discuss each of them.

The photo-electric counting rates C_{ij} are obtained from Eq. (13): $C_{ij} = S_{ij}/t$, where t is the sensor exposure time. It is reasonable to assume that the camera operator selects acquisition settings to ensure that the signal is well into the shot noise regime: $\sigma_{C_{ij}} = \sqrt{S_{ij}}/t$. With signals exceeding 10^4 e$^-$ in 1 s (the case in the examples below), the relative uncertainty on C_{ij} will be below 1 %.

The background signal C_0 is estimated by averaging the pixels looking at the background of the scene. While one would presume that the averaging of a large number of such pixels should yield a very high precision, the accuracy is limited by the difficulty of identifying pixels effectively looking at the background. Automated data processing needs a screening of each image to determine if a pixel is looking at the plume, the background, a cloud or even a bird. This screening is based on the interpretation of the raw signals and, for instance, it sometimes fails to recognize pixels which still have in their FOV the residual NO_2 molecules left by a past position of the plume. From our experience, the relative uncertainty on C_0 determined from a single image is generally larger than 1 % (determined from the sample standard

deviation). Using multiple images, as explained in Sect. 3.3, reduces this uncertainty, as C_0 is computed for each image and then averaged. A 1 % total relative error is achievable with a few images.

The relative instrument response nonuniformity ρ_{ij} can be obtained from a homogeneous scene (i.e., a flat field such that $I_{ij}(\lambda) = I(\lambda)\,\forall i, j$). In this particular case, $\rho_{ij}(\lambda) = C_{ij}(\lambda)/C(\lambda)$, where $C(\lambda)$ is the average of C_{ij} over a large number of pixels. If the flat field is built from a number of relatively homogeneous images under the assumption that their average is truly flat, then the uncertainty on the flatness participates to the error budget of $\rho_{ij}(\lambda)$ and quickly becomes the driver (signal shot noise is surpassed). This error source is a generic problem of all imaging systems but remains difficult to quantify. The only certainty is that it drops with the sample size.

The NO_2 absorption cross-section data are taken from Vandaele et al. (1998), who report a total relative uncertainty of 3 % at a resolution of 2 cm^{-1} (0.04 nm at 450 nm). Taking our coarser resolution into account (about 0.6 nm), the uncertainty drops to about 0.8 % for the convolved spectrum. However, the AOTF tuning curve is temperature dependent, with a typical drift of +0.1 nm per Kelvin (Ohmachi and Uchida, 1970; Uchida, 1971). The driving electronics is currently not enslaved to a temperature sensor. The exact measurement wavelength is computed at the processing stage. Depending on the amount of wavelength drift, the uncertainty on $\sigma_{NO_2}(\lambda)$ can reach 5–10 %.

The minimum relative uncertainty on the NO_2 SCD will be reached if the uncertainty on the plume transmittance T is driven by C_0. Assuming $\sigma_T/T = 1\,\%$, and taking into account a 5 % error on the cross-section term (with a typical value for $\sigma_{NO_2}(\lambda_s) - \sigma_{NO_2}(\lambda_w) = 2 \times 10^{-19}$), one obtains $\sigma_k = 5 \times 10^{16}$ molecules cm^{-2}. If one assumes less favorable conditions like a 1 % uncertainty on ρ, yielding $\sigma_T/T = 2\,\%$ and a 10 % error on the cross section, then the SCD error reaches 10^{17} molecules cm^{-2}.

4 Application to the remote sensing of NO_2 at a coal-fired power plant

The data of a spectral imager such as the NO_2 camera are more easily exploited if a number of observational requirements are satisfied. First, the camera must be placed at a location where both the plume and the background can be captured within the same image. Second, the target plume must remain optically thin in order to preserve the assumption of the Beer–Lambert extinction along a straight light path. Finally, scattered clouds behind the plume will corrupt the retrieval and should be avoided.

These three requirements were sometimes fulfilled during the second Airborne ROmanian Measurements of Aerosols and Trace gases (AROMAT-2) campaign in August 2015. The campaign aimed at joining the efforts of several European research institutes and universities to spatially and temporally characterize the emissions from two types of sites: a large city (Bucharest) and point sources (large thermal power plants in the Jiu Valley, Romania). Both sites should eventually serve as validation targets for the ESA TROPOMI/S-5P mission.

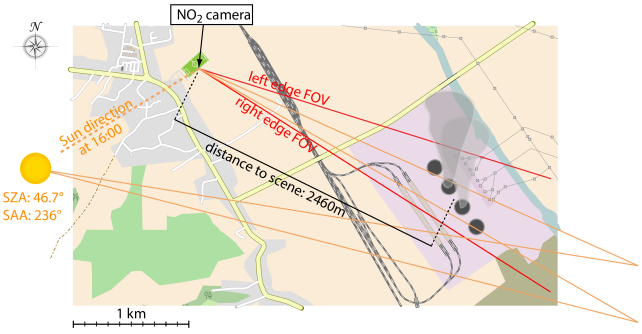

Figure 4. Observational geometry during the AROMAT-2 campaign at Turceni's power plant. The NO_2 camera was installed on a football pitch looking at the four 280 m tall stacks. The red lines delimit the camera horizontal FOV (6°). The direction of the Sun at 16:00 local time is approximately indicated, together with two rays illustrating the scattering behind the scene towards the camera. One of the rays passes through the plume, while the other one passes by. Map data from OpenStreetMap.

The NO_2 camera was placed at a distance of 2.5 km from a group of four stacks belonging to Turceni's power plant, the largest being in Romania (330 MW per turbine, 2000 GWh $year^{-1}$ total electric power generation of which more than 93 % is generated from coal). Figure 4 depicts the measurement geometry. Our location was 44.6792° N, 23.3788° E, the line of sight (LOS) azimuth angle ranged from 113° (left edge of the image) to 119° (right edge) eastward from north, and the LOS zenith angle ranged between 75.5° (top edge) and 81.5° (bottom edge). We only report on measurements performed on 24 August between 16:15 and 16:30 LT as the observational conditions were close to ideal and best illustrate the performance of the instrument. In particular, the smokes were optically thin, with the blue sky clearly visible in the background. This ensures that absorption is the dominant process over scattering for the extinction of light rays crossing the plumes (Beer–Lambert regime). The optical thickness of the smokes was always smaller than 0.1 at our measurement wavelengths.

4.1 Exhaust plume NO_2 SCD field

As explained in Sect. 3.1, the 2-D NO_2 SCD field is computed from at least two spectral images recorded at wavelengths showing a significant difference of absorption cross section. To increase the reliability of the measurements, four doublets of wavelengths were used: $\lambda_{w1} = 441.8$ and $\lambda_{s1} = 439.3$; $\lambda_{w2} = 446.7$ and $\lambda_{s2} = 448.1$; $\lambda_{w3} = 437.9$ and

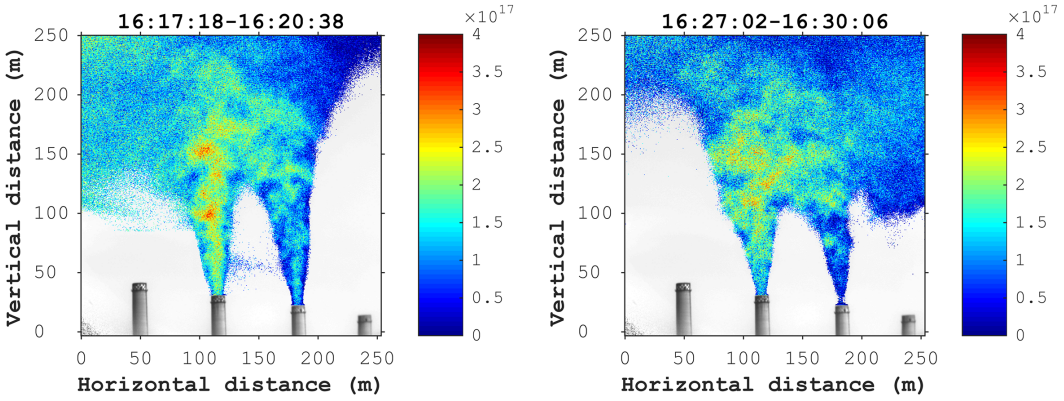

Figure 5. Sample NO_2 SCD field obtained from the averaging of images acquired at $\lambda_{w2} = 446.7$ nm, $\lambda_{s2} = 448.1$ nm, $\lambda_{w4} = 465.8$ nm and $\lambda_{s4} = 463.2$ nm (12 of each). The color scale shows the plume NO_2 SCD in molecules cm^{-2}. The x and y axes show the image dimensions in the scene plane, while the title gives the time span (local time).

$\lambda_{s3} = 435.1$; $\lambda_{w4} = 465.8$ and $\lambda_{s4} = 463.2$. The automated acquisition system was in charge of synchronizing the driving of the AOTF with the image acquisition. A nominal acquisition sequence started by setting the appropriate acoustic signal for the AOTF to filter at λ_{w1}, opening the CCD shutter for 0.5 s, reading out the image and repeating these operations for the seven other wavelengths. After completion of the nominal sequence, a picture with the AOTF turned off is taken and the nominal sequence is resumed. The dwell time between the closing of the shutter and its reopening was 1.3 s, yielding a total acquisition sequence duration of 13.1 s for the 8 spectral images. In the plane of the stacks, the image footprint spans an area of 250×250 m^2 with a 50 cm sampling.

The data analysis revealed that the images from the second and fourth doublets were the less noisy because of a larger natural radiance and sensor sensitivity compared to the wavelengths of doublets 1 and 3. Also, due to the plume displacement over time (wind) and the presence of moving and changing inhomogeneities across the plume (puffs, turbulent eddies), it was necessary to perform time averaging (Sect. 3.3). Indeed, the 1.3 s between two consecutive images is already a long time for features moving at a typical 5 m s^{-1} speed (corresponding to 10 pixels per second).

Figure 5 shows the NO_2 SCD field retrieved from the averaging of images taken at λ_{w2}, λ_{s2}, λ_{w4} and λ_{s4} (12 of each) using the method described in Sect. 3.3. For each wavelength, the background signal C_0 was determined from image areas unaffected by the plume. The relative error on C_0 is about 0.5 % (estimated from the standard deviation σ_{C_0} of the pixels sample yielding C_0). Within this precision, no variation of C_0 across the FOV could be significantly detected. The reason is the relatively small FOV of the camera (about 6°) combined with a high Sun at the time of the measurements (making the scene illumination quite homogeneous). In Fig. 5, the background grayscale image is the mean image at λ_{w4}, whereas the pixels where the SCD is computed were selected based on the criterium $C_{ij} < C_0 - 2\sigma_{C_0}$. Investigating the random fluctuations observed in various areas of the SCD field, one can estimate the detection limit to about 5×10^{16} molecules cm^{-2}.

4.2 NO_2 emission fluxes and synergies with SO_2 cameras

The capability of resolving the NO_2 SCD field with a high spatial and temporal resolution provides new possibilities for the understanding of the plume chemistry. Coal combustion processes yielding the formation of nitrogen and sulfur species are well known (Flagan and Seinfeld, 1988), and several reactive plume models can simulate the transport, formation and removal of these species over different scales. These models are generally validated by in situ air sampling at distances of several kilometers downwind (see for instance Chowdhury et al., 2015). Very few experiments attempted to characterize the reactive content of the early plume, where the reactions are still governed by the combustion products (Hewitt, 2001). In most cases, a DOAS scanning system was used (Lee et al., 2014, 2009; Lohberger et al., 2004). The same technique was also used for SO_2, but to a lesser extent since the introduction of filter-based SO_2 cameras (Smekens et al., 2015). Recently, imaging Fourier transform spectroscopy (IFTS) demonstrated capability for the measurement of a number of mid-infrared emitting species such as CO_2 and SO_2 (Gross et al., 2010). However, NO, but not NO_2, can be retrieved with this technique.

An undisputed advantage of imaging systems with high temporal resolution is their ability to track the displacement of remarkable features from one image to another. We used the complete time series of spectral images (50 sequences of 8 spectral images at a rate of 0.5 Hz) to determine the vertical speed of the plume. This was done by tracking signal features created by local increase or decrease of the NO_2 concentration. On average, a vertical speed of 4.8 ± 0.5 m s^{-1} was ob-

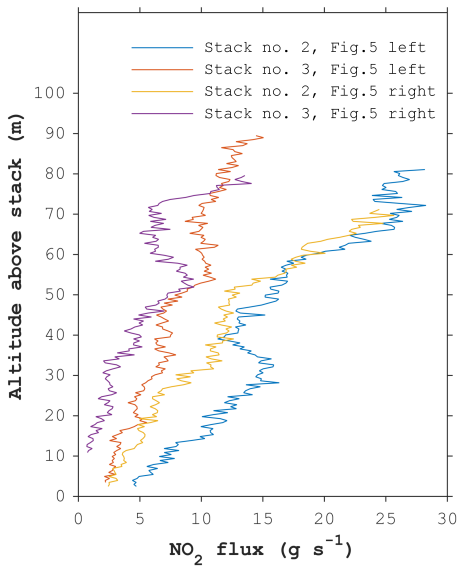

Figure 6. NO_2 flux computed through the plume horizontal cross section as a function of altitude. Stacks height is 280 m. A symmetric Gaussian dispersion is assumed up to the region of apparent intersection of the two plumes.

served. Furthermore, assuming a Gaussian dispersion of the plume, one can infer a circular cross section from the apparent width of the plume at each detector row (i.e., every 50 cm above the stack outlet). As a result, a profile of emission flux (in $g\,s^{-1}$) can be drawn. Figure 6 shows the NO_2 emission flux as a function of altitude up to a height above which the two plumes cannot be discriminated anymore. The fluxes were calculated from the two SCD maps of Fig. 5 and both stacks. The increase is the result of the conversion of NO into NO_2 mainly by the reactions $2NO + O_2 \rightarrow 2NO_2$ and $NO + HO_2 \rightarrow NO_2 + OH$ (Flagan and Seinfeld, 1988; Miller and Bowman, 1989), even if these processes are balanced by the photodissociation of NO_2 as soon as it reaches open air under daylight ($NO_2 + h\nu \rightarrow NO + O$). Qualitatively, these results agree well with the increase reported by Lee et al. (2009) in a study of the rate of increase of NO_2 above power plant stacks. The analysis of Fig. 6 reveals that within the method approximations, the NO_2 concentration in the plume increases at a rate ranging from 0.75 to $1.25\,g\,s^{-1}$ (9.8×10^{21}–1.6×10^{22} molecules s^{-1}) on average for the first 20 s.

The knowledge of the spatial distribution of NO_2 can also prove useful to correct measurements marked by interference from NO_2. A good example is with SO_2 cameras where the SO_2 SCD field is retrieved by comparing the plume transmittance around 310 and 330 nm. In this range, NO_2 is also absorbing and its cross section roughly doubles from 310 to 330 nm. Therefore, if both molecules are present in the plume, the SO_2 camera alone cannot distinguish their respective signatures. So far, this interference has been overlooked in SO_2 camera validation exercises (Smekens et al., 2015; Kern et al., 2010). In the case of the plumes shown in Fig. 5 for instance, a SO_2 camera such as the one used by Smekens et al. (2015) would observe a $\Delta\tau_{NO_2} = 0.04$ when the NO_2 SCD reaches 3×10^{17} molecules cm^{-2}. This variation of optical thickness corresponds to a SO_2 SCD of about 1.6×10^{17} molecules cm^{-2}, which is twice the detection limit reported in Smekens et al. (2015). Clearly, the bias would increase with higher concentrations of NO_2. Taking advantage of the similar spatial resolution of both instruments, the NO_2 camera can provide a complete correction map for the SO_2 data. On the temporal resolution side, however, the NO_2 camera is, at the moment, not capable of following the pace of SO_2 cameras (1 Hz typical), such that the correction maps would have to be applied to temporally averaged SO_2 data.

5 Conclusions

We have described a new passive atmospheric remote sensing instrument for the measurement of NO_2 SCDs above strong sources. It is based on an AOTF which offers a sufficient acceptance angle to be placed in an imaging system and the necessary resolution for taking advantage of the fine structures of the NO_2 absorption cross section. The AOTF is electrically driven, such that fast synchronized acquisitions of spectral images are possible.

The measurement principle is similar to the filter-based SO_2 camera: SCDs are retrieved from at least two spectral images taken at wavelengths where absorption by the target molecule is significantly different. Wavelengths are picked in the range 440–470 nm. Thanks to its higher spectral resolution, the AOTF-based NO_2 camera can perform its measurements within a few nanometers. This makes the sensitivity to aerosols negligibly small.

A mathematical framework for data processing has been developed, and the different sources of error have been addressed. In applications focusing on relatively high spatiotemporal resolution, the NO_2 SCD detection limit is about 5×10^{16} molecules cm^{-2}. Different measurement geometries offering longer integration times or more stable targets would yield a lower limit.

The NO_2 camera was successfully tested during the AROMAT-2 campaign where measurements of NO_2 SCD fields above the flue gas stacks of a coal-fired power plant were performed with a temporal resolution of 3 min and a spatial sampling of 50 cm (for a complete scene of $250 \times 250\,m^2$). Values up to 4×10^{17} molecules cm^{-2} were observed. The quality of the data allowed us to clearly identify the conversion process from NO to NO_2 in the early plume, providing quantitative information on the plume dynamic chemistry. In another example of application, the measurements were used to show how the knowledge of the high-resolution NO_2 field can help to correct SO_2 camera data. If overlooked, the interfering absorption of NO_2 can yield

a significant bias in the retrieved SO_2 SCDs. Other applications range from emission monitoring to volcanic plume chemistry.

While the concept is mature, a number of improvement directions are still being investigated. The most promising ones are the implementation of a temperature feedback loop to reduce the uncertainty on the filtered wavelength and the replacement of the CCD by a CMOS in order to reduce the cooling needs and increase the temporal resolution of the measurements.

6 Data availability

The data are available upon request to the contact author.

Author contributions. Emmanuel Dekemper developed the NO_2 camera measurement principle, led the characterization and the participation in the AROMAT-2 campaign, and processed the data. Bert Van Opstal and Jurgen Vanhamel developed the acquisition software and the AOTF driving electronics and participated in the campaign. Didier Fussen is at the origin of the instrument concept and supported its development in the frame of the ALTIUS project. The authors declare that they have no conflict of interest.

Acknowledgements. This work was funded under PRODEX contract 4000110400. Participation to the AROMAT-2 campaign was funded under ESA contract 4000113511. The authors would like to thank Alexis Merlaud for inviting them to participate in the AROMAT-2 campaign. Emmanuel Dekemper would like to thank Kerstin Stebel for the interesting discussions on SO_2 cameras and Vitaly Voloshinov for his support in all AOTF-related matters.

Edited by: F. Prata
Reviewed by: C. Kern and J.-F. Smekens

References

Bluth, G. J. S., Shannon, J. M., Watson, I. M., Prata, A. J., and Realmuto, V. J.: Development of an ultra-violet digital camera for volcanic SO_2 imaging, J. Volcanol. Geoth. Res., 161, 47–56, doi:10.1016/j.jvolgeores.2006.11.004, 2007.

Chang, I. C.: Noncollinear acousto-optic filter with large angular aperture, Appl. Phys. Lett., 25, 370–372, doi:10.1063/1.1655512, 1974.

Chowdhury, B., Karamchandani, P., Sykes, R., Henn, D., and Knipping, E.: Reactive puff model SCICHEM: Model enhancements and performance studies, Atmos. Environ., 117, 242–258, doi:10.1016/j.atmosenv.2015.07.012, 2015.

Dekemper, E., Loodts, N., Van Opstal, B., Maes, J., Vanhellemont, F., Mateshvili, N., Franssens, G., Pieroux, D., Bingen, C., Robert, C., De Vos, L., Aballea, L., and Fussen, D.: Tunable acousto-optic spectral imager for atmospheric composition measurements in the visible spectral domain, Appl. Optics, 51, 6259–6267, doi:10.1364/AO.51.006259, 2012.

Flagan, R. C. and Seinfeld, J. H.: Fundamentals of Air Pollution Engineering, Prentice Hall, Englewood Cliffs, USA, 1988.

Fussen, D., Dekemper, E., Errera, Q., Franssens, G., Mateshvili, N., Pieroux, D., and Vanhellemont, F.: The ALTIUS mission, Atmos. Meas. Tech. Discuss., doi:10.5194/amt-2016-213, in review, 2016.

Gross, K. C., Bradley, K. C., and Perram, G. P.: Remote identification and quantification of industrial smokestack effluents via imaging fourier-transform spectroscopy, Environ. Sci. Technol., 44, 9390–9397, doi:10.1021/es101823z, 2010.

Heue, K.-P., Wagner, T., Broccardo, S. P., Walter, D., Piketh, S. J., Ross, K. E., Beirle, S., and Platt, U.: Direct observation of two dimensional trace gas distributions with an airborne Imaging DOAS instrument, Atmos. Chem. Phys., 8, 6707–6717, doi:10.5194/acp-8-6707-2008, 2008.

Hewitt, C. N.: The atmospheric chemistry of sulphur and nitrogen in power station plumes, Atmos. Environ., 35, 1155–1170, doi:10.1016/S1474-8177(02)80012-2, 2001.

Kern, C., Kick, F., Lübcke, P., Vogel, L., Wöhrbach, M., and Platt, U.: Theoretical description of functionality, applications, and limitations of SO_2 cameras for the remote sensing of volcanic plumes, Atmos. Meas. Tech., 3, 733–749, doi:10.5194/amt-3-733-2010, 2010.

Lee, H., Kim, Y. J., and Lee, C.: Estimation of the rate of increase in nitrogen dioxide concentrations from power plant stacks using an imaging-DOAS, Environ. Monit. Assess., 152, 61–70, doi:10.1007/s10661-008-0296-4, 2009.

Lee, H., Ryu, J., Jeong, U., Noh, Y., Shin, S. K., Hong, H., and Kwon, S.: Improvement in plume dispersion formulas for stack emissions using ground-based imaging-DOAS data, B. Korean Chem. Soc., 35, 3427–3432, doi:10.5012/bkcs.2014.35.12.3427, 2014.

Lohberger, F., Hönninger, G., and Platt, U.: Ground-based imaging differential optical absorption spectroscopy of atmospheric gases, Appl. Optics, 43, 4711–4717, doi:10.1364/AO.43.004711, 2004.

Lübcke, P., Bobrowski, N., Illing, S., Kern, C., Alvarez Nieves, J. M., Vogel, L., Zielcke, J., Delgado Granados, H., and Platt, U.: On the absolute calibration of SO_2 cameras, Atmos. Meas. Tech., 6, 677–696, doi:10.5194/amt-6-677-2013, 2013.

Miller, J. A. and Bowman, C. T.: Mechanism and modeling of nitrogen chemistry in combustion, Prog. Energy Combust. Sci., 15, 287–338, doi:10.1016/0360-1285(89)90017-8, 1989.

Mori, T. and Burton, M.: The SO_2 camera: A simple, fast and cheap method for ground-based imaging of SO_2 in volcanic plumes, Geophys. Res. Lett., 33, L24804, doi:10.1029/2006GL027916, 2006.

Ohmachi, Y. and Uchida, N.: Temperature Dependence of Elastic, Dielectric, and Piezoelectric Constants in TeO_2 Single Crystals, J. Appl. Phys., 41, 2307–2311, doi:10.1063/1.1659223, 1970.

Platt, U.: Differential Optical Absorption Spectroscopy (DOAS), in: Air Monitoring By Spectroscopic Techniques, edited by: Sigrist, M. W., John Wiley & Sons, Ltd., New York, USA, 1994.

Seinfeld, J. H. and Pandis, S. N.: Atmospheric chemistry and physics, 2nd edn., Wiley, Hoboken, New Jersey, USA, 2006.

Smekens, J.-F., Burton, M. R., and Clarke, A. B.: Validation of the SO2 camera for high temporal and spatial resolution monitoring of SO_2 emissions, J. Volcanol. Geoth. Res., 300, 37–47, doi:10.1016/j.jvolgeores.2014.10.014, 2015.

Uchida, N.: Optical Properties of Single-Crystal Paratellurite (TeO_2), Phys. Rev. B, 4, 3736–3745, doi:10.1103/PhysRevB.4.3736, 1971.

Vandaele, A. C., Hermans, C., Simon, P. C., Carleer, M., Colin, R., Fally, S., Mérienne, M. F., Jenouvrier, A., and Coquart, B.: Measurements of the NO_2 absorption cross-section from 42 000 cm^{-1} to 10 000 cm^{-1} (238–1000 nm) at 220 K and 294 K, J. Quant. Spectrosc. Ra., 59, 171–184, doi:10.1016/S0022-4073(97)00168-4, 1998.

Voloshinov, V. B., Yushkov, K. B., and Linde, B. B. J.: Improvement in performance of a TeO_2 acousto-optic imaging spectrometer, J. Opt. A-Pure Appl. Opt., 9, 341–347, doi:10.1088/1464-4258/9/4/006, 2007.